Expectation Maximisation algorithms for Terahertz transmission tomography

B. Recur[a], H. Balacey[b,c] and P. Mounaix[b]

[a]Australian National University, Dept Applied Maths, RSPE, Canberra, Australia
[b]LOMA, Bordeaux University, CNRS-UMR 5798,
351 cours de la Libération, 33405 Talence, France
[c]Noctylio S.A.S, 59 cours de l'Intendance, 33000 Bordeaux, France

ABSTRACT

Terahertz (THz) tomography is a recently developed imaging technique allowing 3D inspection of opaque objects. In this paper, we develop an ordered subsets convex algorithm for THz transmission tomography (THz-OSC). Since the reconstruction quality is highly depending on the THz beam energy, we investigate afterwards a multi-energy version of the algorithm in order to provide a more accurate reconstruction of the acquired sample. This multi-energy approach is validated by reconstructing data from tomographic acquisitions measured with a 84/287 GHz transmission scanner. Then we discuss how this dual-energy approach could be able to extract physical properties of acquired samples in addition to improving 3D reconstruction.

Keywords: Dual-Energy, Terahertz Tomography, Iterative Reconstructions

1. INTRODUCTION

Terahertz (THz) tomography is now a well-established imaging technique allowing 3D inspection of opaque objects.[1–5] Several radiographs are acquired at different viewing angles around a sample, allowing a 3D tomographic volume reconstruction of the object. High-contrast of low density, and small-size objects, is achieved thanks to the low energy of THz waves. This property has made THz tomography a complementary technique to X-ray CT since such samples provide a low contrast resolution using the latter.

Several reconstruction methods have been investigated for 3D THz tomography.[6,7] However, matter and THz wave interactions are often not taken into account in these techniques, especially those using monochromatic continuous waves (CW). The overall attenuation $\mu(x)$ in each voxel x of the reconstructed volume is proportional to the different scatterings of the THz waves in the object. During the last decades, X-Ray dual-energy tomography has been developed to recover material characteristics (typically density $\rho(x)$ and atomic number $Z(x)$) by combining two energy acquisitions.[8–11] This material characterisation is based on a separate modelling of photoelectric effect and Compton scattering which are the main interactions of X-ray radiations with matter.

Similar 3D material characterisation has never been investigated with a CW-THz setup. In this paper we investigate a more realistic propagation model of THz/matter interactions. We develop a 3D tomographic acquisition setup and a reconstruction method able to combine several monochromatic acquisitions. Using data acquired with a dual-energy 84/287 GHz scanner, we explore how this reconstruction is able to extract physical properties in addition to the 3D reconstruction, and we discuss about feasibility, current limitations and aspiring benefits of such an approach. The paper is thus organized as follows: Section 2 details the tomographic reconstruction algorithm. Section 3 describes the associated acquisition setup allowing dual-energy measurements. Qualitative, quantitative and chemical analysis are discussed before concluding in section 4.

Further author information: (Send correspondence to B. Recur)
B. Recur: E-mail: benoit.recur@anu.edu.au,
H. Balacey: E-mail: hugo.balacey@gmail.com,
P. Mounaix: E-mail: p.mounaix@loma.u-bordeaux1.fr

Terahertz Emitters, Receivers, and Applications V, edited by Manijeh Razeghi, Alexei N. Baranov, John M. Zavada, Dimitris Pavlidis, Proc. of SPIE Vol. 9199, 91990O · © 2014 SPIE
CCC code: 0277-786X/14/$18 · doi: 10.1117/12.2062476

2. THZ TOMOGRAPHIC RECONSTRUCTION ALGORITHM

Before developing the order subset convex (OSC) algorithm for THz transmission tomography, we first present the basics of the OSC method and detail how to take into account the specific Gaussian propagation of THz beam in the forward model of the algorithm. Then we detail how reconstructed data could allow one to estimate material distribution using multiple monochromatic-wave acquisitions at different energies.

2.1 Ordered subset convex algorithm

Expectation maximization algorithms refer to a class of tomographic reconstruction techniques, for computing the 3D structural volume of a sample from a set of its radiographs. The expectation to observe measurements R of a given sample μ, denoted $p(R|\mu)$, follows a Poisson distribution:

$$p(R|\mu) = \prod_i \frac{\mathrm{e}^{-\hat{R}(i)}(\hat{R}(i))^{R(i)}}{R(i)!} \tag{1}$$

where i is a projection line index. The expected photon counts $\hat{R}$ at detector position i is defined by:

$$\hat{R}(i) = I_0(i)\mathrm{e}^{-\sum_j w_{ij}\mu(j)} + bg(i) \tag{2}$$

where I_0 is the maximal photon counts (measured without sample), bg is the background noise (dark-field) and w_{ij} is a weight coefficient defining the voxel j contribution on the detector i (usually proportional to the distance crossed by line i in voxel j). I_0 and bg are determined experimentally. Based on the probability $p(R|\mu)$ and the transmission model $\hat{R}$, reconstruction method consists of maximizing the log likelihood $L = \log p(R|\mu)$. The solution can be achieved by the Newton-Raphson algorithm iterating in t:[12–14]

$$\mu_{t+1} = \mu_t - \frac{\partial_{\mu_t} L}{\partial^2_{\mu_i^2} L} \tag{3}$$

2.2 Gaussian beam modelling

Contrary to X-rays, THz propagation follows a Gaussian distribution depending on the THz wave properties, and the lens used to focus the beam. The radius of the beam (from the beam axis) has its minimum value w_0 at the beam waist (cf. Fig. 1). At the wavelength λ, the radius at distance z from the beam waist is:

$$w(z) = w_0\sqrt{1 + \left(\frac{z}{z_R}\right)^2} \tag{4}$$

where $z_R = \frac{\pi w_0^2}{\lambda}$ is the Rayleigh range. Moreover, the cross-section of the intensity distribution is given by:

$$G(j) = I_{\max}\left(\frac{w_0}{w(z)}\right)^2 \exp\left(\frac{-2r^2}{w^2(z)}\right) \tag{5}$$

where j is the 3D position vector at distance r from the beam axis, and z from the beam waist, and $I_{\max}$ is the intensity of beam waist centre. As an illustration, Fig. 1 (a-b) shows the Gaussian distribution at beam waist (measured $w_0 = 2.3$mm at FWHM), and the beam propagation of a 287 GHz source. Thus in the remainder of the paper, $\hat{R}(i)$ is no longer defined by Eq. 2 but by the following formula:

$$\hat{R}(i) = I_0(i)\mathrm{e}^{-\sum_j w_{ij}\mu(j)\star G(j)} + bg(i) \tag{6}$$

where $\star$ denotes the convolution operator and $G(j)$ is defined by Eq. 5.

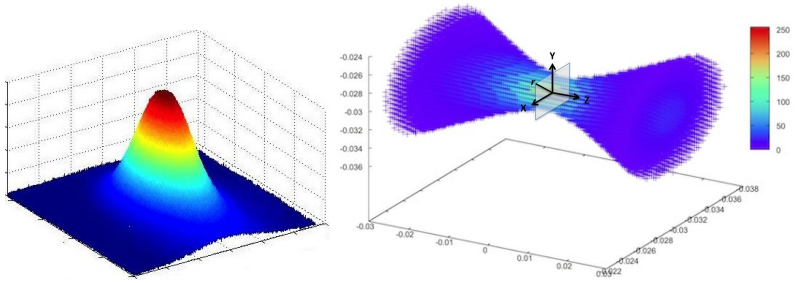

(a) (b)

Figure 1. (a) Gaussian intensity distribution at beam waist (Intensity (a.u)). (b) Simulated propagation of the beam for a 287 GHz source (position in meters), $w_0 = 2.3$ mm at beam waist (FWHM) according to previously measured beam.

2.3 Penalization part

In addition to $p(R|\mu)$, we have used a penalization term $p(\mu)$ to regularize the solution. $p(\mu)$ is defined with respect to the Gaussian distribution of reconstructed data by:[15]

$$p(\mu) = e^{-\beta \sum_j \sum_{k \in \mathcal{N}(j)} y_{jk} \Phi(\mu(j) - \mu(k))} \tag{7}$$

where β is a relaxation parameter, $\mathcal{N}(j)$ denotes the neighbourhood of pixel j, $\Phi(\cdot)$ is a potential function and y_{jk} is a weight factor (usually inverse proportional to the distance between voxels j and k). In this paper, we use the following LogCosh potential function:[16]

$$\Phi(x) = 2\gamma t^2 \log\cosh\left(\frac{|x|}{t}\right) \tag{8}$$

where γ is a sensitivity parameter. This potential attenuates the small variations between neighbourhood reconstructed voxels, increasing homogeneity of the regions and preserving the edges beyond the given threshold t. Using $L = \log[p(R|\mu)p(\mu)]$ in Eq. (3), the overall penalized ordered subsets convex algorithm for THz tomography (THz-OSC) consists of iterating over t and subsets $s+1$, in order to update each voxel j of the volume μ until convergence of the solution:

$$\mu_{s+1}^t(j) = \mu_s^t(j) + \alpha^t \frac{\sum_{i \in S(s)} w_{ij} \left[\hat{R}_s^t(i) - R(i)\right] - \beta \sum_{k \in \mathcal{N}(j)} y_{jk} \Phi'\left[\mu_s^t(j) - \mu_s^t(k)\right]}{\sum_{i \in S(s)} w_{ij} \left(\sum_l w_{il}\right) \hat{R}_s^t(i) + \beta \sum_{k \in \mathcal{N}(j)} y_{jk} \Phi''\left[\mu_s^t(j) - \mu_s^t(k)\right]} \tag{9}$$

where $\hat{R}_s^t(i)$ is the expected photon counts computed from μ_s^t using Eq. (6), α^t is a relaxation parameter, $S(s)$ are the radiographs in the subset s and $\Phi'(\cdot)$ and $\Phi''(\cdot)$ are respectively the first and second derivative of $\Phi(\cdot)$. The volume obtained at subset s is used as starting volume of the next subset $s+1$. A main iteration t is completed when all subsets have been processed.

2.4 Towards a material characterisation using multiple CW-THz acquisitions

The THz-OSC reconstruction algorithm provides the 3D local attenuation $\mu_\nu(x)$ which depends on the beam frequency ν used for the acquisition. In the THz range this attenuation is mainly proportional to the extinction coefficient $\mathcal{K}$ (neglecting optical effects):

$$\mathcal{K}_\nu(x) = \frac{c}{4\pi\nu}\mu_\nu(x). \tag{10}$$

$\mathcal{K}_m(\nu)$ for all $\nu \in [0.1 \cdots 10$ THz$]$ of an elementary chemical m can be measured using time-domain spectroscopy (TDS). TDS measurements thus allow one to create a dictionary of all material coefficients. Such a

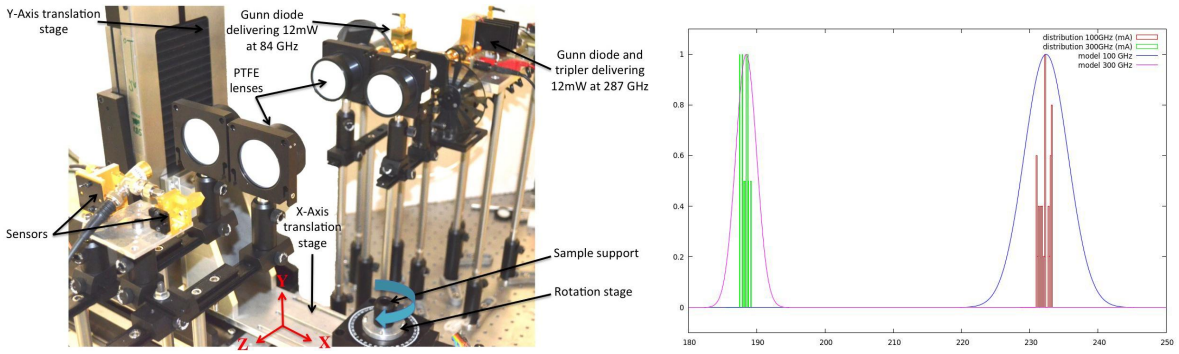

(a) (b)

Figure 2. (a) Experimental setup: THz beams delivered by a pair of Gunn diodes at 84 GHz and 287 GHz are collimated and focused by a pair of PTFE lenses. The sample is positioned on a three-axis motorized stage, allowing X,Y and θ movement. (b) Blank scan distribution : measured distribution at 84 GHz and 287 GHz respectively in green and red boxes are approximated by a Normal distribution (*resp.* in purple and blue).

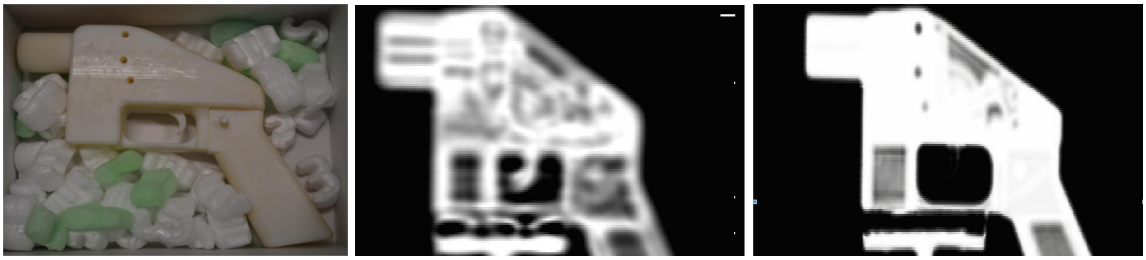

(a) (b) (c)

Figure 3. (a) Original sample: a plastic-gun. (b) 84 GHz projection. (c) 287 GHz projection.

dictionary could be used to estimate the chemical composition of each voxel of a 3D volume obtained by CW-THz acquisitions, leading to a 3D reconstruction labelled/segmented material by material. Thus in addition to the THz-OSC algorithm, we investigate a dual-energy acquisition performed at two distinct frequencies ν_1 and ν_2. Then we discuss if the associated dual reconstruction of volumes $(\mu_{\nu_1}, \mu_{\nu_2})$ is able to provide an estimate of chemical composition using a material database obtained by TDS measurements.

3. EXPERIMENTAL SETUP

The experimental setup is composed of two Gunn diodes, each coupled with a horn antenna (cf. Fig. 2(a)). They deliver an output power of 12 mW at $\nu_1 = 84$ GHz and $\nu_2 = 287$ GHz respectively. The THz beams are collimated and focused with a pair of PTFE lenses ($f = 50$ mm focal length and $D = 50.8$ mm). Detection is performed with a Schottky diode, and each beam is modulated at 1 kHz by a mechanical chopper. The amplitude of the transmitted THz signal is acquired with a lock-in amplifier. The sample is positioned on a three-axis motorized stage allowing X,Y and θ movement. 2D transmission radiographs at ν_1 and ν_2 are measured by moving the object along the X and Y axes, with a scan step of 1mm in both directions. Overall acquisition is composed of a dual set (ν_1, ν_2) of 2D projections uniformly distributed between 0° and 180°. As an example, Fig. 3(b-c) shows the 84 GHz and 287 GHz projections of a plastic-gun (Fig. 3(a)).

In order to process the line acquisition Eq. (6) in the THz-OSC algorithm, both the blank scan I_0 and dark-field bg have to be determined. The blank scan is estimated for each energy by measuring THz source response on the detector. The normalized distribution of the 84 GHz and 287 GHz responses are depicted by the box-histograms on Fig. 2(b). These distributions can be modeled by a normal distribution $\mathcal{N}(\bar{I}_0, \sigma_{I_0})$. We have estimated $\bar{I}_0(84\text{GHz}) = 232.40$ mA and $\sigma_{I_0}(84\text{GHz}) = 4.53$; and $\bar{I}_0(287\text{GHz}) = 188.45$ mA and $\sigma_{I_0}(287\text{GHz}) = 2.17$ for the 84GHz and 287GHz sources, respectively. Similarly we have estimated the dark-field distribution as $\mathcal{N}(\bar{bg} = -0.00780, \sigma_{bg} = 0.00035)$ by measuring the detector response when THz source

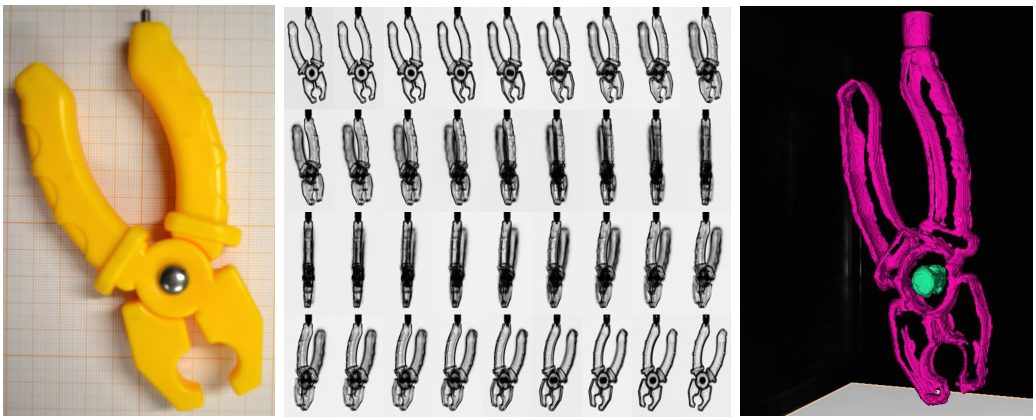

(a) (b) (c)

Figure 4. (a) Picture of the scanned pliers. (b) 36 projections of the sample acquired uniformly across the angle range $[0°, 180°]$, with an angular step of $5°$ between two consecutive projections. (c) 3D visualisation of the reconstructed object.

is inactive. Due to the very low standard deviations, we have set clear-fields and dark-field to $I_0(i) = \bar{I_0}$ and $bg(i) = \bar{bg}$ for all i in the following analysis.

4. RESULTS AND DISCUSSION

In this section we first discuss the quality of the THz-OSC algorithm compared to other standard methods. This study includes a quantitative analysis based, on a processing sequence allowing area and volume measurements on reconstructed data. Finally we discuss the potential of 3D multi-energy CW-THz imaging for chemical reconstruction/segmentation, using a chemical database obtained by TDS.

4.1 Qualitative analysis

The qualitative analysis in this section focuses on the reconstruction quality achieved by the THz-OSC algorithm, compared to two other algorithms: the standard filtered backprojection (FBP) and the Simultaneous Algebraic Reconstruction Technique (SART) for THz tomography.[7] We base our discussion on the 287 GHz acquisition of the plastic pliers with a metallic axes shown on Fig. 4(a). The sample is imaged at 36 projections with translation step of 0.5mm in both X and Y directions (cf. Fig. 4(b)), leading to a reconstructed volume voxel size of 0.125mm^3 (cf. Fig. 4(c)).

Figure 5 shows a set of 6 cross-sectional images along the Y-Axis obtained by the standard FBP, the THz-SART reconstruction and the THz-OSC method, respectively. The SART result is obtained after 3 iterations. THz-OSC convergence is obtained after 10 iterations using 4 subsets. Increases in reconstruction time are negligible compared to the acquisition time. First we can notice that the reconstructed object is surrounded by many artifacts in the FBP results. This method is particularly sensitive to the noise and it is unable to reconstruct accurately from a small number of projections. Even if SART quality seems better, one can note the presence of few streak artifacts (high intensity lines), especially in the slices containing the metallic axis ($y \in [160..240]$). The transmission model used in the THz-OSC method leads to more uniform reconstructed intensities: the inner and outer parts of the object are recovered more accurately. Moreover, neither background noise or streak artifacts are visible in the reconstruction.

4.2 Quantitative analysis

A 3D segmentation is applied using a K-mean algorithm[17,18] in order to separate the reconstructed volume into k clusters of voxels, such that all the voxels of a cluster minimize the within-sum of square. This method extracts the object of interest from the background and remaining acquisition/reconstruction noise. Cluster(s) corresponding to the object are then processed by a component labelling technique to obtain the different components of the

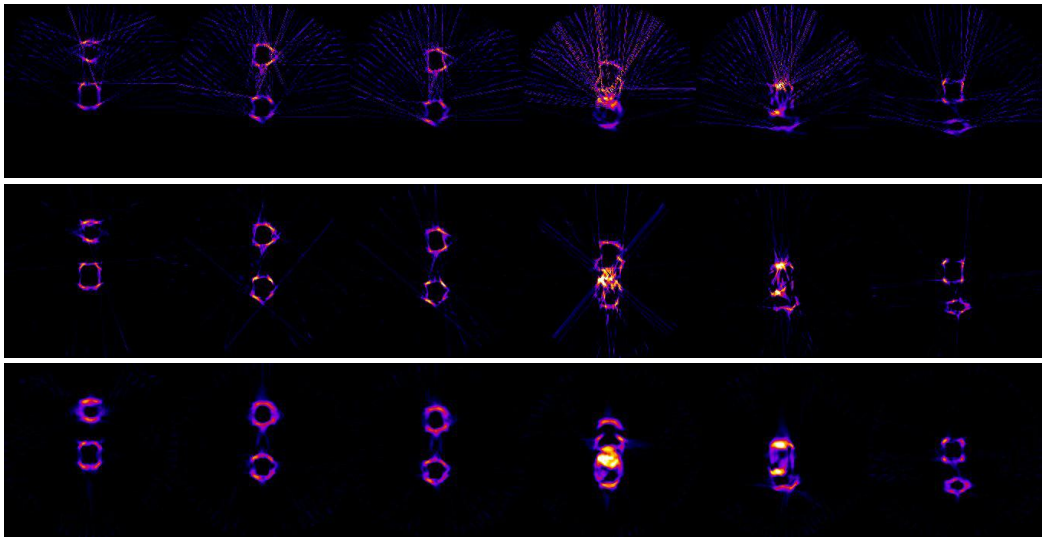

Figure 5. Cross-sections along Y-Axis of the imaged object obtained respectively by BFP, THz-SART and THz ML-TR methods (from the top to bottom line, respectively). From left to right: $y = 60, 100, 140, 180, 220$, and 260.

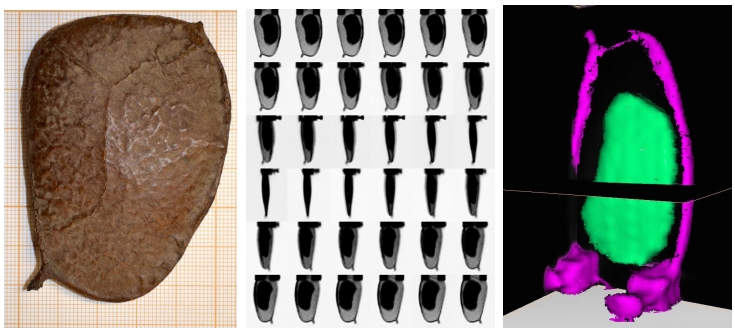

(a) (b) (c)

Figure 6. (a) Picture of the fruit kernel. (b) 36 projections of the fruit kernel acquired uniformly in the range $[0°, 180°]$ with an anuglar step of $5°$ between two consecutive projections. (c) 3D visualisation of the reconstructed object where a part of the skin appears in purple, and the interior seed is clearly identified in green.

object. As an illustration, the 3D visualisation Fig. 5(c) shows the labelled plastics and metallic parts in purple and green, respectively. Similar processing has been applied on the dried kernel fruit shown on Fig. 6.

Some numeric data can be computed from labelled regions such as: the surface area, determining a ROI, and ROI volumes (cf. Tab. 1). However, such surface and volume measurements only quantify the object ROIs which have been reconstructed from radiographs. Since THz waves suffer from multiple optical effects,[19–22] contrast in low-absorption parts of the object becomes negligible. Then, the averaging performed during the tomographic reconstruction leads to almost invisible ROIs (corresponding to the object parts which are very transparent to THz waves on several viewing angles) even if these ROIs seem visible in the projections. All these reasons explain why the outer part of the fruit kernel and of the pliers are not entirely reconstructed.

4.3 Towards a material-based segmentation

As mentioned in section 2.4, a chemical characterisation could be performed on reconstructed volume supposing that each value $\mu_\nu(x)$ at voxel x is proportional to the extinction coefficient (cf. Eq. 10). No TDS measurements are available for the chemicals composing the fruit kernel and pliers. Thus, we are not able to verify possible matching in a material dictionary. Conversely, we have measured the absorption and extinction coefficients of

Sample	Area (cm^2)	Volume (cm^3)
Fruit (outer part)	23.67	1.837
Fruit (kernel)	32.80	2.353
Pliers (plastics)	174.43	10.945
Pliers (metallic axis)	6.437	0.489

Table 1. Component characteristics: surface-area and volume quantizations.

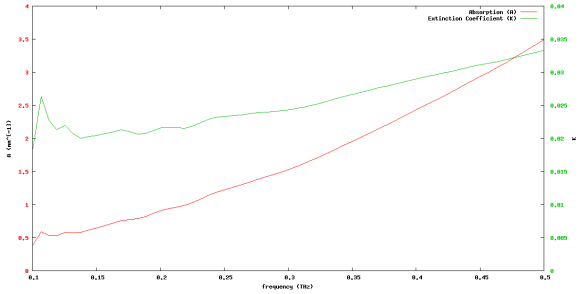

(a)

Values ($\times 10^{-3}$)	84 GHz	287 GHz
$\mathcal{K}_{TDS}$	18.42	24.06
$\mathcal{K}_{\nu_i}$	16.57	24.23
$\sigma\left(\mathcal{K}_{\nu_i}\right)$	5.16	5.93
MSE (single energy)	30.07	35.17
MSE (cumulated)	32.63	

(b)

Figure 7. (a) Absorption and extinction coefficient of the chemical (resin) composing the plastic-gun sample, according to the THz frequency (between 0.1 and 0.5 THz). (b) Theoretical extinction coefficients obtained by TDS measurements compared to the coefficients computed from reconstructed volumes of the plastic-gun.

the chemicals composing the plastic-gun Fig. 3 using TDS (cf. Fig. 7(a)). After reconstruction using the THz-OSC algorithm, plastic-gun volumes have been segmented using the processing sequence introduced in previous section, extracting the ROI corresponding to the object only. Then we have computed the average $\mathcal{K}$ values of the ROI at each frequency (cf. Table in Fig. 7(b)). One can remark that $\mathcal{K}_{287\text{GHz}} = 24.23$ is very close to the theoretical value $\mathcal{K}_{TDS} = 24.06$. $\mathcal{K}_{84\text{GHz}} = 16.57$ is less accurate since, $\mathcal{K}_{TDS} = 18.42$. However this latter value corresponds to the extinction coefficient at 100 GHz since our TDS setup does not provide values below this frequency. Even if the reconstructed average values seem close to the TDS measurements, they are not very accurate as illustrated by their standard deviations $\sigma(\mathcal{K}_{\nu_i})$. Thus MSE computed between reconstructed voxels and theoretical values (set to $\mathcal{K}_{TDS}$) show non-negligible errors which could penalize a material characterisation. These limitations are mainly due to the fact that optical effects are neglected in the forward processing of the reconstruction method (Eq. 6).

5. CONCLUSION

In this paper we have proposed an expectation maximization algorithm based on the ordered-subsets convex (OSC) method, in order to reconstruct 3D images from CW-THz acquisitions. This algorithm reconstructs the 3D attenuation (or the extinction) coefficient of the sample, by including a Gaussian propagation model of the THz beam. Reconstructed data quality is better compared to standard FBP or algebraic reconstruction techniques, allowing us to perform a dimensional quantitative analysis of acquired data. Finally we have demonstrated that 3D values are in line with those measured by Time-Domain Spectroscopy. These first results let us believe that we could combine the 3D reconstructions from a set of CW-THz acquisitions with a material characterisation based on a chemical dictionary given by TDS. However the reconstructed value distributions of a single-chemical sample highlight new limitations of the reconstruction. These limitations include optical effects which are neglected in the forward model of the iterative reconstruction. Thus we will investigate in our future works dual 3D reconstruction / 3D chemically based segmentation, and optimization of the forward processing by including more realistic optical effect models.

REFERENCES

[1] Wang, S., Ferguson, B., Abbott, D., and Zhang, X.-C., "T-ray imaging and tomography," *Journal of Biological Physics* **29**(2-3), 247–256 (2003).

[2] Wang, S. and Zhang, X., "Pulsed terahertz tomography," *Journal of Physics D: Applied Physics* **37**(4), R1 (2004).
[3] Awad, M. and Cheville, R., "Transmission terahertz waveguide-based imaging below the diffraction limit," *Applied Physics Letters* **86**(22), 221107–221107 (2005).
[4] Yin, X., Ng, B. W.-H., Ferguson, B., and Abbott, D., "Wavelet based local tomographic image using terahertz techniques," *Digital Signal Processing* **19**(4), 750–763 (2009).
[5] Brahm, A., Kunz, M., Riehemann, S., Notni, G., and Tünnermann, A., "Volumetric spectral analysis of materials using terahertz-tomography techniques," *Applied Physics B* **100**(1), 151–158 (2010).
[6] Recur, B., Younus, A., Salort, S., Mounaix, P., Chassagne, B., Desbarats, P., Caumes, J.-P., Abraham, E., et al., "Investigation on reconstruction methods applied to 3d terahertz computed tomography," *Optics Express* **19**(6), 5105–5117 (2011).
[7] Recur, B., Guillet, J.-P., Manek-Hönninger, I., Delagnes, J.-C., Benharbone, W., Desbarats, P., Domenger, J.-P., Canioni, L., Mounaix, P., et al., "Propagation beam consideration for 3d thz computed tomography," *Optics Express* **20**(5), 5817–5829 (2012).
[8] Alvarez, R. E. and Macovski, A., "Energy-selective reconstructions in x-ray computerised tomography," *Physics in medicine and biology* **21**(5), 733 (1976).
[9] Siddiqui, S. and Khamees, A. A., "Dual-energy ct-scanning applications in rock characterization," in [*SPE Annual Technical Conference and Exhibition (Society of Petroleum Engineers, 2004), paper*], (2004).
[10] Heismann, B., Leppert, J., and Stierstorfer, K., "Density and atomic number measurements with spectral x-ray attenuation method," *Journal of applied physics* **94**(3), 2073–2079 (2003).
[11] Nuyts, J., De Man, B., Fessler, J. A., Zbijewski, W., and Beekman, F. J., "Modelling the physics in the iterative reconstruction for transmission computed tomography," *Physics in medicine and biology* **58**(12), R63 (2013).
[12] Lange, K. and Fessler, J. A., "Globally convergent algorithms for maximum a posteriori transmission tomography," *Image Processing, IEEE Transactions on* **4**(10), 1430–1438 (1995).
[13] De Man, B., Basu, S., Thibault, J.-B., Hsieh, J., Fessier, J., Bouman, C., and Sauer, K., "A study of four minimization approaches for iterative reconstruction in x-ray ct," in [*Nuclear Science Symposium Conference Record, 2005 IEEE*], **5**, 2708–2710, IEEE (2005).
[14] Kamphuis, C. and Beekman, F. J., "Accelerated iterative transmission ct reconstruction using an ordered subsets convex algorithm," *Medical Imaging, IEEE Transactions on* **17**(6), 1101–1105 (1998).
[15] Geman, S. and McClure, D. E., "Statistical methods for tomographic image reconstruction," (1987).
[16] Green, P. J., "Bayesian reconstructions from emission tomography data using a modified em algorithm," *Medical Imaging, IEEE Transactions on* **9**(1), 84–93 (1990).
[17] MacQueen, J. et al., "Some methods for classification and analysis of multivariate observations," in [*Proceedings of the fifth Berkeley symposium on mathematical statistics and probability*], **1**(14), 281–297, California, USA (1967).
[18] Hartigan, J. A. and Wong, M. A., "Algorithm as 136: A k-means clustering algorithm," *Applied statistics* , 100–108 (1979).
[19] Abraham, E., Younus, A., Aguerre, C., Desbarats, P., and Mounaix, P., "Refraction losses in terahertz computed tomography," *Optics Communications* **283**(10), 2050–2055 (2010).
[20] Hérault, É., Hofman, M., Garet, F., and Coutaz, J.-L., "Observation of terahertz beam diffraction by fabrics," *Optics letters* **38**(15), 2708–2710 (2013).
[21] Li, Y.-D., Li, Q., She, J.-Y., and Wang, Q., "Investigation on diffraction characteristics of continuous terahertz beam limited by hard-edge apertures," *Optik-International Journal for Light and Electron Optics* **124**(22), 5669–5673 (2013).
[22] Brahm, A., Wilms, A., Tymoshchuk, M., Grossmann, C., Notni, G., and Tünnermann, A., "Optical effects at projection measurements for terahertz tomography," *Optics & Laser Technology* **62**, 49–57 (2014).